Active Damping Control of Linear Hybrid Stepping Motor for Cogging Force Compensation

Tai-Sik Hwang[1], Jul-Ki Seok[1], and Dong-Hun Kim[2]

[1]Power Conversion Laboratory, School of Electrical Engineering, Yeungnam University, Kyungbuk, Korea
[2]School of Electrical Engineering and Computer Science, Kyungpook University, Daegu, Korea

Linear hybrid stepping motors (LHSMs) have a simple structure and provide ripple-free holding force at the aligned position. Despite these attractive features, however, an LHSM delivers strong thrust vibrations during position-to-position movement that are the dominant cause of the positioning error, mechanical stress, and acoustic noise. In order to overcome this defect, we have developed an active control scheme to damp the vibration of a $\pi/4$-multiple-pitched LHSM by a feed-forward compensation signal. Utilizing an elaborate reluctance network based on the finite-element analysis to take the nonlinear magnetic properties into account, we model the LHSM with force ripple components as a nonlinear position-dependent function. We estimate the damping force signal from the Jacobian linearization observer. The positioning accuracy is significantly improved through a closed-loop control scheme for restraining the thrust ripple.

***Index Terms*—Active control scheme, closed-loop control, feed-forward compensation, linear hybrid stepping motors (LHSMs), thrust vibrations.**

I. Introduction

THE development of high-speed and high-precision motion control systems has been an active area of research for the past few years due to the increasing demand on higher productivity and better product quality in the advanced manufacturing industries such as semiconductor process, high-precision machinery, etc. Compared to traditional drives for rotational electro-motors using screw or toothed belts, the direct-drive linear motors exhibit the higher reliability, longer lifetime, less friction, and no backlash, resulting in high accuracy for linear motion.

Among the various electric linear motors, the linear hybrid stepping motors (LHSMs) are naturally thought to be the most suitable for the applications requiring high speed, low cost, and simple control [1]. Most LHSMs consist of a permanent magnet (PM) mover with coil windings and a platen with many teeth. From this hybrid topology, LHSMs produce a high force density and deliver the ripple-free holding force at aligned position. However, despite the attractive features, the LHSMs have the significant thrust vibrations during position-to-position movement due to the space harmonics of the permeance distributed over the air gap [2].

In a case of the smooth control required especially at low speed, such as the image observation system using a camera mounted directly on LHSMs or servo applications, the reduction of the force ripple becomes the main issue because the mechanical vibrations of LHSMs at high speed are filtered out by the mechanical system. The periodic thrust ripples at low speed cause position error by more than 30 μm, mechanical vibration, and acoustic noise, that make the control performance worse and sometimes result in destruction of the systems. Consequently, their use in servo systems which require smooth/quiet operation and accurate position control of less than 5 μm at low speeds has been limited.

Until now, two primary approaches have been attempted for reducing the force pulsations: One method is to improve the magnetic design of the motor [3] and the other is to use sophisticated modern control theory [4]. An interesting design structure employing dual PM topology was proposed in [3], where all the magnetic poles of a motor have the permeances with $\pi/4$-multiple pitch difference. Because of the tendency of aligning two PMs along the direction of minimum reluctance, the cogging forces in the opposite direction cancel each other so that the total pulsation is weakened. Even adopting the dual PM topology, the LHSM still contains the cogging force generated by design imperfections and nonlinear magnetic nonlinearity of the practical motor that are assumed to mainly yield nonsinusoidal flux distribution in the air gap. Nevertheless, the $\pi/4$-multiple-pitched LHSM with inherently low detent force is a strong candidate for high-performance motion control applications.

An alternative approach to the high-performance control was explored via Kalman filtering in order to estimate the precise position of LHSMs without a position sensor [4]. Unfortunately, the method is not based on the actual motor modeling with thrust force oscillations and not easy to be implemented because of its complexity and a burden of huge computing time required. Thus, in order to realize high-precision control performance in all operating range, the force ripple effects should be suppressed using an online closed-loop control based on the accurate modeling of the motor considered.

This paper proposes a new active ripple-reduction scheme adapted to a change of the operating point of LHSMs. Utilizing an elaborate reluctance network based on the FE analysis to take the design imperfections and nonlinear magnetic characteristics into account, it is confirmed that the dominant components of force vibration are position-dependent low-order harmonics from a fundamental to the fourth-order harmonic. In the proposed analysis, the nonlinear model for an LHSM including the periodic disturbances is formulated mathematically.

Digital Object Identifier 10.1109/TMAG.2005.860961

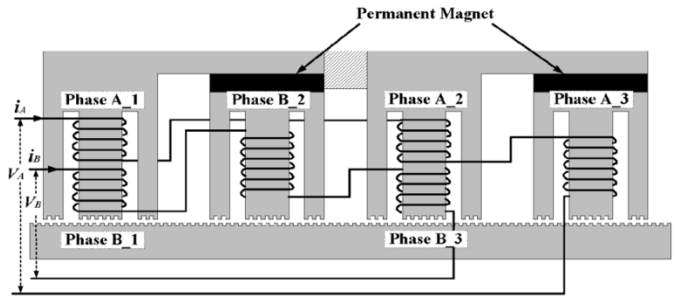

Fig. 1. Structure of $\pi/4$-multiple-pitched LHSM.

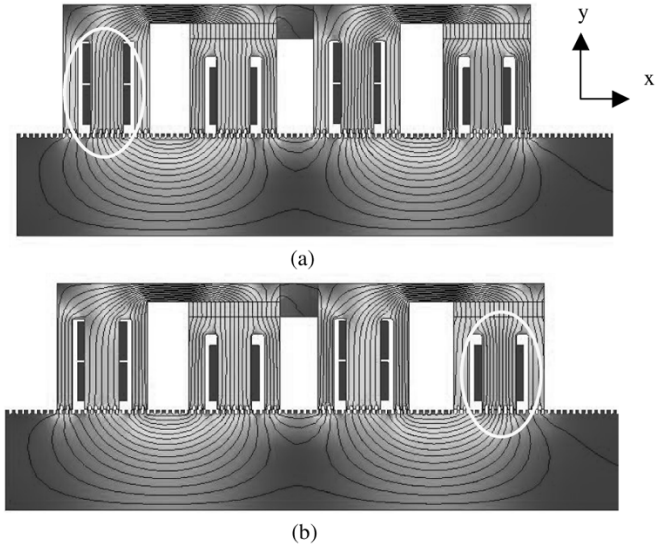

Fig. 2. Contours of magnetic flux density. (a) Alignment between the first pole and platen teeth (b) Alignment between the fourth pole and platen teeth.

The damping signal at an arbitrary mover position is dynamically estimated from the Jacobian linearization observer and is adaptively injected so as to cancel the force ripple by feed-forward manner. The control strategy advocated here is shown to be robust to the design imperfections and magnetic nonlinearity of the motor. Experimental results are also presented to prove the effectiveness of the proposed vibration-rejecting scheme.

II. Causes of Magnetic Imbalances

The schematic of $\pi/4$-multiple-pitched LHSM is shown in Fig. 1, where the residual flux density of the PM with its magnetization upward is 1.145 T. The first and third magnetic poles have a two-phase coil winding structure, respectively and each phase coil turn is $1/\sqrt{2}$ times those of main windings wound at the second and forth poles. Such the compound windings are revealed to make an enhancement in the force-producing characteristic of the LHSMs [3].

For an elaborate reluctance network taking into account the magnetic imbalance and nonlinear property of the LHSM, the two-dimensional finite element analysis (FEA) is carried out by using a commercial software package called MagNet VI. In order to investigate magnetic field distribution and flux linkage of each coil winding during one stroke of 1 mm, the PM mover without current excitation is set to move over the platen along the x direction [Fig. 2]. This will lead us to better understanding of the force ripple phenomenon mainly generated by inherently

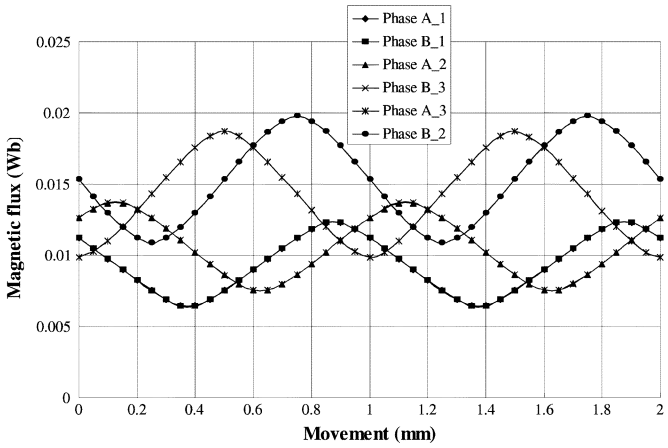

Fig. 3. Comparison of linkage flux of each coil windings.

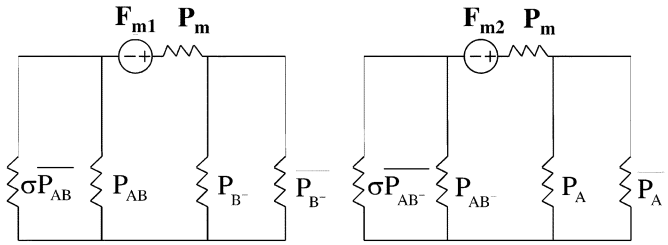

Fig. 4. Modified magnetic circuit with magnetic asymmetry.

unbalanced magnetic structure of the LHSM at low speed. Fig. 2 shows the comparison of magnetic field distributions at two specified positions during the movement of the mover. It is apparently noticed that there is a meaningful difference between the two cases even though each pole teeth marked in a circle are exactly aligned with the platen ones. The difference is thought to result from the undesirable magnetic coupling between two main magnetic flux paths of the LHSM that is often assumed to be separated to each other. To quantify the effect of the magnetic imbalance, the flux linking of each coil winding is computed in Fig. 3 where the polarity of each winding is ignored for easy comparison between them. It shows that amplitude of the flux linkage of three windings located on the right of the LHSM is always bigger by almost 6% than that of the rest windings on the left.

Therefore, for a more accurate prediction of the thrust ripple, the magnetic imbalance of the LHSM has to be properly reflected in the reluctance network method.

III. Modeling and Active Damping Control Scheme

A. LHSM Modeling With Magnetic Asymmetry

To consider the asymmetry of flux distribution properly, it is desirable to assign two different magnetic motive force (F_{m1} and F_{m2}) and insert a branch with asymmetric factor, σ, in the original magnetic circuit [3] as shown in Fig. 4 where P_m represents the permeance of the PM.

Neglecting high-order harmonic components [5], the permeance in each branch is given by

$$P_{AB} = P_o + \sum_{n=1}^{5} P_n \cos n\left(\theta - \frac{\pi}{4}\right) \tag{1}$$

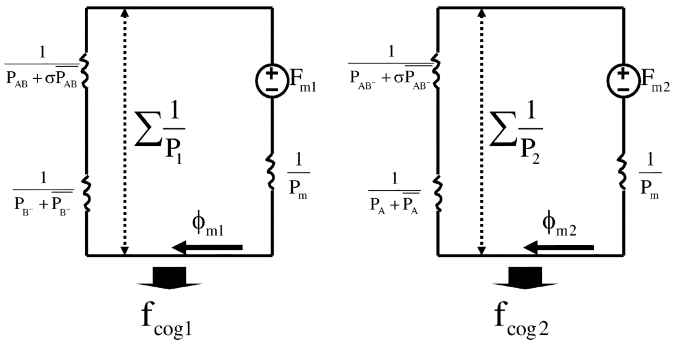

Fig. 5. Simplified magnetic equivalent circuit.

$$\overline{P_{AB}} = P_o + \sum_{n=1}^{5} P_n \cos n\left(\theta - \frac{\pi}{4} - \pi\right) \tag{2}$$

$$P_{B^-} = P_o + \sum_{n=1}^{5} P_n \cos n\left(\theta - \frac{\pi}{2}\right) \tag{3}$$

$$\overline{P_{B^-}} = P_o + \sum_{n=1}^{5} P_n \cos n\left(\theta - \frac{\pi}{2} - \pi\right) \tag{4}$$

$$P_{AB^-} = P_o + \sum_{n=1}^{5} P_n \cos n\left(\theta - \frac{3\pi}{4}\right) \tag{5}$$

$$\overline{P_{AB^-}} = P_o + \sum_{n=1}^{5} P_n \cos n\left(\theta - \frac{3\pi}{4} - \pi\right) \tag{6}$$

$$P_A = P_o + \sum_{n=1}^{5} P_n \cos n(\theta - \pi) \tag{7}$$

$$\overline{P_A} = P_o + \sum_{n=1}^{5} P_n \cos n(\theta) \tag{8}$$

$$\theta = \gamma x = \frac{2\pi}{p_t} x \tag{9}$$

where p_t is the pole pitch and x indicates the mover position.

A simplified magnetic circuit is redrawn as shown in Fig. 5 under the conditions of $P_o \gg (\sigma-1)/(\sigma+1)P_1$ and $P_o \gg P_2, P_3, P_4, P_5$ [4]. Then, the total permeance can be calculated as

$$\frac{1}{\sum P_1} \cong \frac{1}{P_o^2} \begin{pmatrix} \frac{\sigma+3}{2(\sigma+1)} P_o - \frac{\sigma-1}{(\sigma+1)^2} P_1 \cos\left(\theta - \frac{\pi}{4}\right) \\ + \frac{P_2}{2}\cos 2\theta - \frac{P_2}{\sigma+1}\sin 2\theta \\ - \frac{\sigma-1}{(\sigma+1)^2} P_3 \cos\left(3\theta - \frac{\pi}{4}\right) - \frac{\sigma-1}{2(\sigma+1)} P_4 \cos 4\theta \end{pmatrix} \tag{10}$$

$$\frac{1}{\sum P_2} \cong \frac{1}{P_o^2} \begin{pmatrix} \frac{\sigma+3}{2(\sigma+1)} P_o - \frac{\sigma-1}{(\sigma+1)^2} P_1 \cos\left(\theta + \frac{\pi}{4}\right) \\ - \frac{P_2}{2}\cos 2\theta + \frac{P_2}{\sigma+1}\sin 2\theta \\ - \frac{\sigma-1}{(\sigma+1)^2} P_3 \cos\left(3\theta + \frac{\pi}{4}\right) - \frac{\sigma-1}{2(\sigma+1)} P_4 \cos 4\theta \end{pmatrix}. \tag{11}$$

Utilizing the above permeance expressions of (10) and (11), the stored magnetic coenergy, W'_{m1} and W'_{m2}, in two circuits of Fig. 5 can be easily obtained as $(F_{m1}P_m)^2/(2\sum P_1)$ and $(F_{m2}P_m)^2/(2\sum P_2)$, respectively.

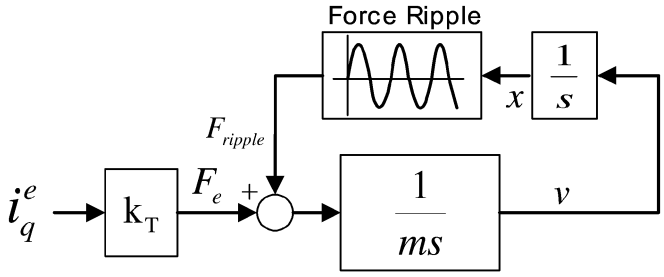

Fig. 6. Block diagram of LHSM model with ripple force effect.

After taking the partial derivative to the stored coenergy, the cogging force generated by each part of the LHSM considered is given by

$$\begin{aligned} f_{\text{cog1}} &= \frac{\partial W'_{m1}}{\partial x} \\ &= \left(\frac{2\pi}{p_t}\right)\frac{\phi^2{}_{m1}}{2P_o^2} \begin{pmatrix} \frac{\sigma-1}{(\sigma+1)^2} P_1 \sin\left(\theta - \frac{\pi}{4}\right) \\ - P_2 \sin 2\theta - \frac{2P_2}{\sigma+1}\cos 2\theta \\ + \frac{3(\sigma-1)}{(\sigma+1)^2} P_3 \sin\left(3\theta - \frac{\pi}{4}\right) \\ + \frac{2(\sigma-1)}{\sigma+1} P_4 \sin 4\theta \end{pmatrix} \end{aligned} \tag{12}$$

$$\begin{aligned} f_{\text{cog2}} &= \frac{\partial W'_{m2}}{\partial x} \\ &= \left(\frac{2\pi}{p_t}\right)\frac{\phi^2_{m2}}{2P_o^2} \begin{pmatrix} \frac{\sigma-1}{(\sigma+1)^2} P_1 \sin\left(\theta + \frac{\pi}{4}\right) \\ + P_2 \sin 2\theta + \frac{2P_2}{\sigma+1}\cos 2\theta \\ + \frac{3(\sigma-1)}{(\sigma+1)^2} P_3 \sin\left(3\theta + \frac{\pi}{4}\right) \\ + \frac{2(\sigma-1)}{\sigma+1} P_4 \sin 4\theta \end{pmatrix}. \end{aligned} \tag{13}$$

The resultant force of the LHSM with the magnetic asymmetry has the form of

$$\begin{aligned} F_{\text{ripple}} &= f_{\text{cog1}} + f_{\text{cog2}} \\ &= f_1 \cos(\gamma x + \delta_1) + f_2 \cos(2\gamma x + \delta_2) \\ &\quad + f_3 \cos(3\gamma x + \delta_3) + f_4 \cos(4\gamma x + \delta_4). \end{aligned} \tag{14}$$

The first, second, third, and fourth-order harmonic components of the permeance generate the same order ripple force and its corresponding amplitude is proportional to the magnetic imbalance.

Using the position-dependent ripple force model, the mechanical equation of the motor is established as

$$\frac{dv}{dt} = \frac{1}{m}(F_e + F_{\text{ripple}}) \tag{15}$$

where v is the motor velocity, m indicates the system mass, and F_e represents the instantaneously generated force. A block diagram of the LHSM model to take into account the ripple force effect is presented in Fig. 6, where k_T denotes the force constant.

To suppress force disturbance, the ripple components need to be observed from currents, velocity feedback, and mechanical

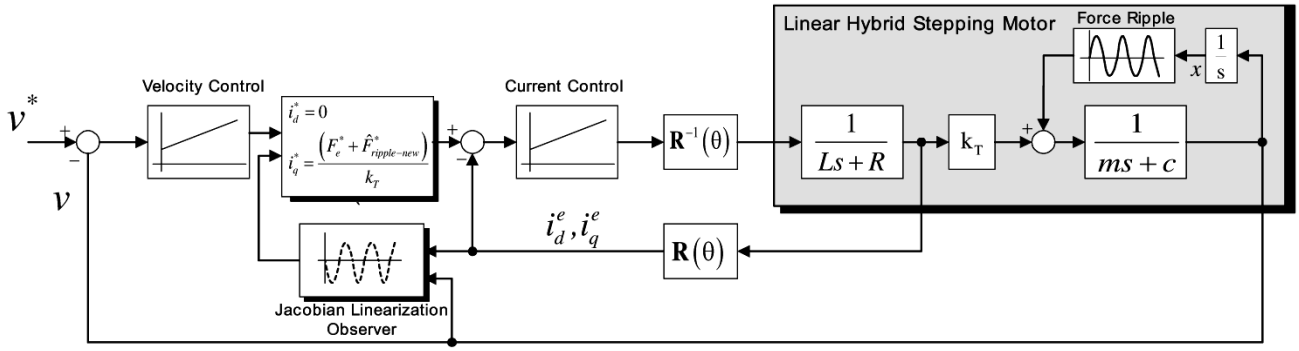

Fig. 7. Overall control block diagram for ripple force reduction.

parameters of the motor. For the purpose of designing an observer, a state-space representation is first required. From (15), the first-order component is described as

$$\begin{aligned} x_1 &= v \\ x_2 &= f_1 \cos(\gamma x + \delta_1) \\ x_3 &= -\frac{f_1}{\gamma} \sin(\gamma x + \delta_1). \end{aligned} \tag{16}$$

The next nonlinear state-space form can be derived from (16)

$$\begin{aligned} \dot{x}_2 &= -\gamma v f_1 \sin(\gamma x + \delta_1) = \gamma^2 x_1 x_3 \\ \dot{x}_3 &= -v f_1 \cos(\gamma x + \delta_1) = -x_1 x_2. \end{aligned} \tag{17}$$

Then, the overall state equation can be obtained with a straightforward extension

$$\begin{aligned} \dot{\boldsymbol{x}} &= f(\boldsymbol{x}) + g(\boldsymbol{x})u \\ y &= h(\boldsymbol{x}) \\ f(\boldsymbol{x}) &= \begin{bmatrix} \frac{1}{m}(x_2 + x_4 + x_6 + x_8) \\ \gamma^2 x_1 x_3 \\ -x_1 x_2 \\ 4\gamma^2 x_1 x_5 \\ -x_1 x_4 \\ 9\gamma^2 x_1 x_7 \\ -x_1 x_6 \\ 16\gamma^2 x_1 x_9 \\ x_1 x_8 \end{bmatrix}, \\ g(\boldsymbol{x}) &= \begin{bmatrix} \frac{1}{m} \\ 0 \\ 0 \\ 0 \\ 0 \\ 0 \\ 0 \\ 0 \\ 0 \end{bmatrix}, \quad h(\boldsymbol{x}) = x_1 \\ F_{\text{ripple}} &= x_2 + x_4 + x_6 + x_8. \end{aligned} \tag{18}$$

B. Active Damping Control Scheme

Contrary to linear systems, the nonlinear observer problem of (18) has not yet been wholly solved in the general sense and there are several particular classes of nonlinear estimation solutions [6]. Here, we choose the Jacobian linearization observer which is designed as (19) by using the first-order linear approximation of the system at the origin

$$\begin{aligned} \dot{\hat{x}}_1 &= \frac{1}{m}(\hat{x}_2 + \hat{x}_4 + \hat{x}_6 + \hat{x}_8) + \frac{1}{m} k_T i_q^e + k_1(y - \hat{x}_1) \\ \dot{\hat{x}}_2 &= \gamma^2 y \hat{x}_3 + k_2(y - \hat{x}_1), \quad \dot{\hat{x}}_3 = -y\hat{x}_2 \\ \dot{\hat{x}}_4 &= 4\gamma^2 y \hat{x}_5 + k_3(y - \hat{x}_1), \quad \dot{\hat{x}}_5 = -y\hat{x}_4 \\ \dot{\hat{x}}_6 &= 9\gamma^2 y \hat{x}_7 + k_4(y - \hat{x}_1), \quad \dot{\hat{x}}_7 = -y\hat{x}_6 \\ \dot{\hat{x}}_8 &= 16\gamma^2 y \hat{x}_9 + k_5(y - \hat{x}_1), \quad \dot{\hat{x}}_9 = -y\hat{x}_8 \\ \hat{F}_{\text{ripple}} &= \hat{x}_2 + \hat{x}_4 + \hat{x}_6 + \hat{x}_8 \end{aligned} \tag{19}$$

where $K = [k_1 \ k_2 \ k_3 \ k_4 \ k_5]^T$ is chosen such that $(\delta f)/(\delta x)(0) + K(\delta h)/(\delta x)(0)$ is a Hurwitz matrix [7]. This observer design method requires neither an integration of partial differential equation nor the knowledge of the input derivatives. That leads to the advantage of easy implementation of the proposed method.

As the velocity increases, the frequency of high-order force ripple is apt to reach the bandwidth of the current controller, ω_c. The phenomenon is undesirable because a generated force, $F_{\text{ripple\_high}}(x)$, for high-order harmonics rejection can easily contain the errors due to the current controller dynamics, i.e.,

$$F_{\text{ripple\_high}}(x) = \frac{\omega_c}{s + \omega_c} \hat{F}_{\text{ripple}}(x). \tag{20}$$

Thus, to cancel out the effect of the controller dynamics, the force ripple command should be changed as

$$\begin{aligned} \hat{F}^*_{\text{ripple\_new}}(x) &= \hat{F}_{\text{ripple}}(x) \times \frac{s + \omega_c}{\omega_c} \\ &= \hat{F}_{\text{ripple}}(x) + \frac{s}{\omega_c} \hat{F}_{\text{ripple}}(x). \end{aligned} \tag{21}$$

In the time-domain, the modified force command is expressed as

$$\hat{F}^*_{\text{ripple\_new}}(x) = \hat{F}_{\text{ripple}}(x) + \frac{1}{\omega_c} \left[\frac{d}{dt} \hat{F}_{\text{ripple}}(x) \right]. \tag{22}$$

It deserves special emphasis that this control function can improve the transient compensation performance as well as the steady-state operations. Fig. 7 shows the overall control block diagram of the proposed scheme to mitigate the ripple force. In the proposed method, the compensating signal is added to the output of PI controller, in a velocity control loop, that adjusts automatically the motor currents to reduce the force pulsation.

TABLE I
RATINGS AND KNOWN PARAMETERS OF LHSM UNDER TEST

Ratings and Parameters	Value
Pole Pitch	1.0[mm]
Coil Resistance	1.4[Ω]
Self Inductance	1.7[mH]
Mass	2.3[kg]
Permanent Magnet	NdFeB (1.145[T])
Rated Static Force	40[N]

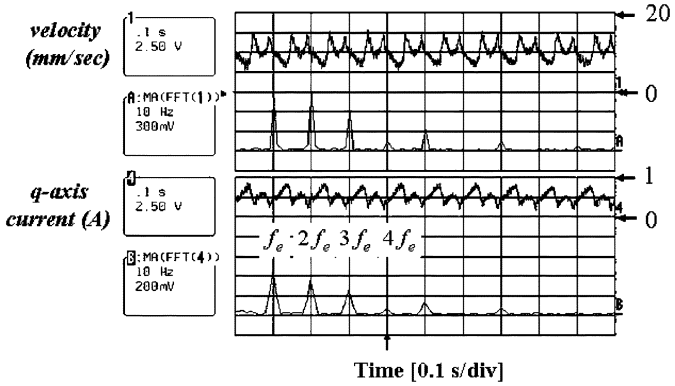

Fig. 8. Test result at 10 mm/s without active damping control.

IV. EXPERIMENTAL RESULTS

The 1 mm-pole-pitch LHSM in Table I was tested to prove the validity of the proposed method. The PWM VSI inverter used here consists of 20 kHz switching devices and is controlled by the control board using a digital signal processor, TMS320VC33-120 MHz. The sampling period of current and speed control loop is 50 and 500 μs, respectively. Then, the bandwidth of velocity and current controller is set to 500 and 5000 rad/s, respectively. The on-line Jacobian observer is performed every 50 μs and the linear encoder with 2000 pulse/pitch resolution is attached to the motor for the closed-loop velocity control. The ADXL-103 accelerometer of Analog Device with the maximum level of ± 1.7 g ($1\text{g} = 9.8$ m/s^2) and 2.5 kHz frequency range is mounted on the moving plate to just monitor the actual motor force.

Fig. 8 shows the experimental result on the velocity and q-axis current feedback at 10 mm/s without the active damping control. In the test, the velocity level is set to be low enough to ensure that the vibration is not filtered out by the mechanical constant. From the top, the velocity and q-axis current feedback are depicted. From the FFT analysis, it is evident that the first, second, third, and fourth-order harmonic components are dominant, and the measurements show a good agreement with the reluctance network and FEM analysis. The frequency spectrum contains the higher order components than the fourth-order one, that are mainly caused by the unmodeled high-order term in permeance, tracking error under control, and inverter dead-time effect.

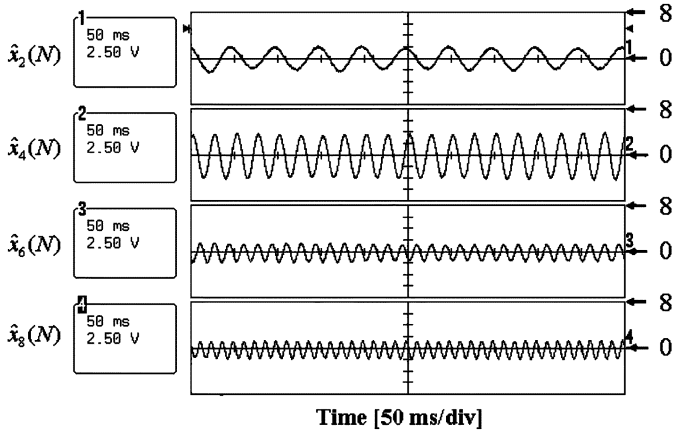

Fig. 9. Estimated ripple force components by proposed observer at 20 mm/s.

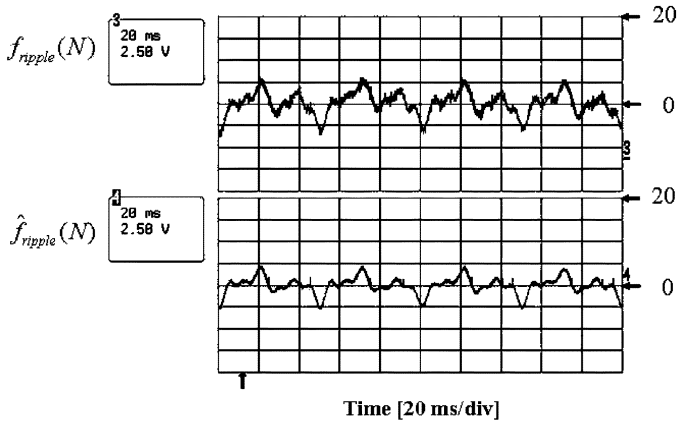

Fig. 10. Comparison between measured and estimated ripple force.

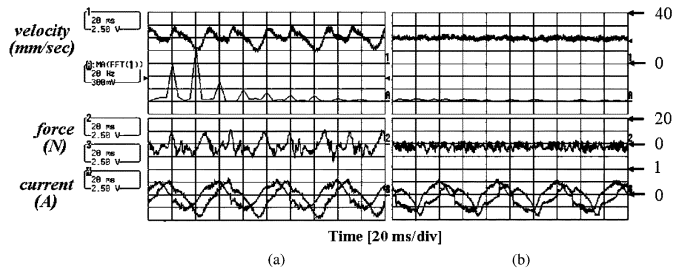

Fig. 11. Ripple force rejection performance at 20 mm/s. (a) Without active damping control (b) With active damping control.

Fig. 9 shows the ripple force components estimated by the proposed real-time observer at 20 mm/s. It is observed that the frequencies of the estimated ripple are integer multiples of a fundamental frequency 20 Hz. To assess how close the estimated force ripple matches the "true" one detected by the accelerometer, the two ripples are compared with each other as illustrated in Fig. 10, where a close match is found except the transient peak region. It is concluded that the proposed algorithm can provide the reliable estimation performance in a real situation.

Fig. 11 presents the comparison of the results on the ripple force rejection performance with or without the active damping control at 20 mm/s. From the top, the velocity, motor force, and phase currents are depicted. At first glance, the phase currents in both cases seem to be quite similar. In practice, however, the

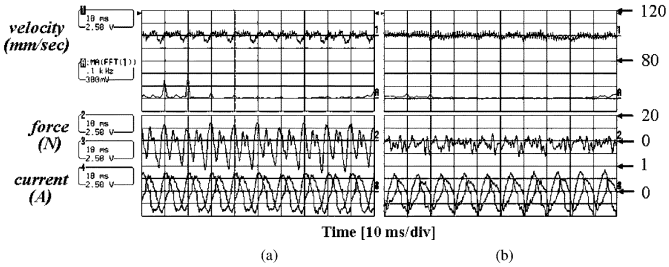

Fig. 12. Ripple force rejection performance at 50 mm/s. (a) Without active damping control (b) With active damping control.

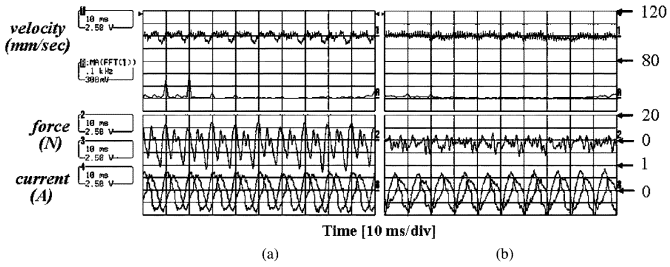

Fig. 13. Ripple force rejection performance at 100 mm/s. (a) Without active damping control (b) With active damping control.

phase currents without the active damping control exhibit compensation delay due to the feedback control alone and this approach is not suited to cover the full critical range of ripple-force frequencies. On the contrary, the currents in feed-forward compensation scheme are almost in anti-phase to the force ripple of the motor. Hence, the proposed algorithm anticipates the disturbances and so yields well-damped velocity/force response compared to the feedback control alone.

Figs. 12 and 13 demonstrate the comparisons between the conventional PI control and the proposed control scheme of mitigating the ripple force when the motor is running at 50 and 100 mm/s, respectively. As expected, at a higher velocity, the velocity ripple amplitude decreases because the ripple is effectively filtered out by mechanical dynamics compared to that running at a lower speed. However, the force in (a) is still fluctuating and this effect results in the acoustic noise emissions. In (b), the estimated disturbance is added to the overall input to cancel the effect of the ripple force with a feed-forward manner. It makes remarkable improvement of the steady-state performance and the reduction of acoustic noise level. The experimental results show that the proposed controller is able to effectively compensate the detent force, unbalanced effect, and other nonlinear characteristics of the LHSM.

The left plot of Fig. 14 illustrates the position tracking error performance for PI control compensation alone and the steady-state errors of more than 40 μm can be seen, that are unacceptable in general servo applications. Compared to the case with PI compensation, close inspection of the tracking errors in the right plot shows that maximum amplitude greatly reduced to less than ± 5 μm. The host position controller is connected to the drive to

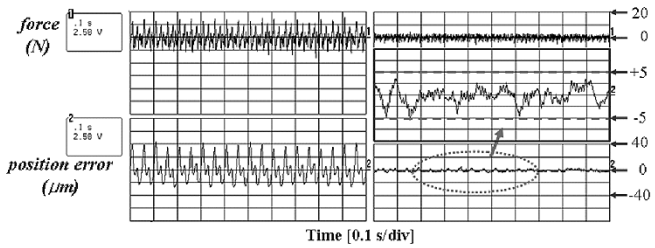

Fig. 14. Position tracking error. (a) Without active damping control. (b) With active damping control.

provide the position command in this test. Employing the proposed compensation method, we are able to achieve positioning accuracy which is within the limits of the servo applications. This is considered a very significant performance improvement by high-performance servo drive makers.

V. Conclusion

A ripple force estimation system has been designed to compensate the inherent mechanical vibration of $\pi/4$-multiple-pitched LHSM. Utilizing the force ripple analysis of the LHSM via the reluctance network and FEM approach, a nonlinear LHSM model with mechanical vibrations and accurate disturbance observer is developed. From the experimental results, it is concluded that the proposed method can cope well with the ripple force problem of the LHSM and it is effective even when the LHSM is applied in servo control applications.

Acknowledgment

This work was supported by KESRI(R-2005-B-143), which is funded by the Ministry of Commerce, Industry and Energy (MOCIE).

References

[1] B. C. Kuo, *Theory and Applications of Step Motors*. New York: West, 1974.

[2] S. Yang, F. Lin, and M. Chen, "Micro-stepping control of a two-phase linear stepping motor with three-phase VSI inverter for high-speed applications," *IEEE Trans. Ind. Appl.*, vol. 40, no. 5, pp. 1257–1264, Sep./Oct. 2004.

[3] J. K. Seok and T. S. Hwang, "Cogging force reduction of two phase linear hybrid stepping motor," *IEEE Trans. Magn.*, vol. 41, no. 6, pp. 2202–2204, Jun. 2005.

[4] J. Hirai, T. Kim, and A. Kawamura, "Position-sensorless drive of linear pulse motor for suppressing transient vibration," *IEEE Trans. Ind. Electron.*, vol. 47, no. 2, pp. 337–345, Apr. 2000.

[5] N. Matsui, M. Nakamura, and T. Kosaka, "Instantaneous torque analysis of hybrid stepping motor," *IEEE Trans. Ind. Appl.*, vol. 32, no. 5, pp. 1176–1182, Sep./Oct. 1996.

[6] N. H. Jo and J. H. Seo, "A state observer for nonlinear systems and its application to ball and beam system," *IEEE Trans. Autom. Control.*, vol. 45, no. 5, pp. 968–973, May 2000.

[7] H. K. Khalil, *Nonlinear Systems*. Englewood Cliffs, NJ: Prentice-Hall, 1996.

Manuscript received August 30, 2005; revised October 27, 2005 (e-mail: doljk@yu.ac.kr).